

Performance of the high-resolution atmospheric model HRRR-AK for correcting geodetic observations from spaceborne radars

W. Gong,¹ F. J. Meyer,¹ P. Webley,¹ and D. Morton²

Received 8 May 2013; revised 4 September 2013; accepted 6 October 2013; published 29 October 2013.

[1] Atmospheric phase delays are considered to be one of the main performance limitations for high-quality satellite radar techniques, especially when applied to ground deformation monitoring. Numerical weather prediction (NWP) models are widely seen as a promising tool for the mitigation of atmospheric delays as they can provide knowledge of the atmospheric conditions at the time of Synthetic Aperture Radar data acquisition. However, a thorough statistical analysis of the performance of using NWP production in radar signal correction is missing to date. This study provides a quantitative analysis of the accuracy in using operational NWP products for signal delay correction in satellite radar geodetic remote sensing. The study focuses on the temperate, subarctic, and Arctic climate regions due to a prevalence of relevant geophysical signals in these areas. In this study, the operational High Resolution Rapid Refresh over the Alaska region (HRRR-AK) model is used and evaluated. Five test sites were selected over Alaska (AK), USA, covering a wide range of climatic regimes that are commonly encountered in high-latitude regions. The performance of the HRRR-AK NWP model for correcting absolute atmospheric range delays of radar signals is assessed by comparing to radiosonde observations. The average estimation accuracy for the one-way zenith total atmospheric delay from 24 h simulations was calculated to be better than ~14 mm. This suggests that the HRRR-AK operational products are a good data source for spaceborne geodetic radar observations atmospheric delay correction, if the geophysical signal to be observed is larger than 20 mm.

Citation: Gong, W., F. J. Meyer, P. Webley, and D. Morton (2013), Performance of the high-resolution atmospheric model HRRR-AK for correcting geodetic observations from spaceborne radars, *J. Geophys. Res. Atmos.*, 118, 11,611–11,624, doi:10.1002/2013JD020170.

1. Introduction and Motivation

[2] Fine resolution and repeatable geodetic measurements are required to precisely measure movements and deformations of the Earth's surface that are triggered by various geophysical phenomena including volcanoes [Dzurisin, 2007; Lu et al., 2010], permafrost [Liu et al., 2010], earthquakes [Segall, 2010; Wei et al., 2010], tidal motion [Eineder et al., 2011], and ground-water extraction [Kampes, 2006]. Precise knowledge of the magnitude and spatial patterns of these surface deformation signals allows determination and quantification of geophysical parameters [Segall, 2010] and

will improve our understanding of the dynamics of the Earth's interior [Sleep and Fujita, 1997].

[3] Despite a large number of successful case studies, the performance and applicability of synthetic aperture radar (SAR) as a geodetic measurement tool is limited by the influence of electromagnetic path delay variations when the signal is propagating through the atmosphere [Richter and Hitney, 1980]. While atmospheric delays can be decomposed into two parts, tropospheric delays and ionospheric delay [Hanssen, 2001; Resch, 1980], this study is focusing on the mitigation of tropospheric delays only.

[4] The majority of the research on atmospheric mitigation methods for geodetic radar remote sensing observations has so far focused on the correction of Interferometric SAR (InSAR) observations. InSAR techniques measure the spatial and temporal derivative of the SAR signal phase in order to extract surface deformation. Due to the double-differencing procedure, atmospheric artifacts in InSAR data are mainly caused by the spatiotemporal variation of atmospheric water vapor while other atmospheric delay components largely cancel out. Mitigation methods often rely on water vapor measurements from external sources such as dense networks of Global Positioning System (GPS) stations [Li et al., 2006a; Onn and Zebker, 2006; Xu et al., 2011] and spaceborne multi-spectral scanners [Li et al., 2009]. Alternative methods are using time series of SAR imagery to filter atmospheric artifacts

¹Geophysical Institute, University of Alaska Fairbanks, Fairbanks, Alaska, USA.

²Arctic Region Supercomputing Center, University of Alaska Fairbanks, Fairbanks, Alaska, USA.

Corresponding author: W. Gong, Earth and Planetary Remote Sensing group, Geophysical Institute, University of Alaska Fairbanks, 903 Koyukuk Dr., West Ridge Research Bldg. 106A.5, Fairbanks, AK 99775, USA. (gwenyu@alaska.edu)

©2013 The Authors. *Journal of Geophysical Research: Atmospheres* published by Wiley on behalf of the American Geophysical Union. This is an open access article under the terms of the Creative Commons Attribution-NonCommercial-NoDerivs License, which permits use and distribution in any medium, provided the original work is properly cited, the use is non-commercial and no modifications or adaptations are made. 2169-897X/13/10.1002/2013JD020170

based on the spatiotemporal statistics of atmospheric water vapor distributions [Berardino et al., 2002; Ferretti et al., 2001]. Besides InSAR, geodetic observations have also been derived using tracking techniques or the recently developed absolute ranging method. Tracking methods identify and track features or noise patterns through sequences of images to determine surface motion. With high-resolution radar systems, tracking methods [Eineder et al., 2011] can detect range changes at the centimeter level, requiring accurate atmospheric correction to produce reliable surface motion measurements. The absolute ranging technique has become applicable since the launch of the TerraSAR-X radar system and allows for the retrieval of precise absolute range measurements between satellite and ground. Absolute ranging can measure geodetic signals like tectonic deformation from only one image but requires precise correction for absolute atmospheric delay for the method to succeed [Eineder et al., 2011].

[5] In the past few years, Numerical Weather Prediction (NWP) simulations have become a novel data source for atmospheric correction of remote sensing data. Many studies have analyzed the merit of NWPs for atmospheric correction of InSAR data [Foster et al., 2013; Fournier et al., 2011; Gong et al., 2010; Webley et al., 2002] and have found that NWPs are often able to correct for effects related to atmospheric stratification [Liu and Hanssen, 2009]. However, results are inconclusive when it comes to correcting for atmospheric turbulence patterns. While only few studies have addressed the correction of atmospheric delays for absolute ranging and tracking techniques, some of them demonstrated up to 3.2 cm ranging accuracy in slant range when using European Centre for Medium-Range Weather Forecasts (ECMWF) for absolute range phase correction [Cong et al., 2012]. In all studies, more thorough statistical analyses are necessary to quantify the performance of NWPs under a range of atmospheric conditions. The goal of our study is the qualification and quantification of the correction performance of the High Resolution Rapid Refresh (HRRR) over the Alaska region (HRRR-AK) based on the Weather Research and Forecasting (WRF) model. HRRR-AK performance is analyzed by a comparison of its predictions to a large number of radiosonde observations (RAOBS) acquired over five test sites in high-latitude regions twice a day and for 16 months. Predictions and observations are compared using statistical methods, and differences between them are analyzed for their dependence on the model lead time, time of day, season, as well as geographic/climatologic properties of the test sites. Study areas have been defined within Alaska, USA, for three reasons (1) Alaska provides a large number of geophysical signals including volcanoes, glacier, and tectonic motion and is therefore a natural test site for geodetic observations from space; (2) as arctic and subarctic environments are more and more becoming the focus of many radar-based remote sensing studies, this study is relevant to a large number of geophysical research questions; (3) with the HRRR-AK, an operational high-resolution NWP is available for Alaska. HRRR-AK is the Alaska-centered adaptation of the 48 contiguous United States High Resolution Rapid Refresh (HRRR) operational atmospheric model. The HRRR-AK model is developed, maintained, and ran at the University of Alaska Fairbanks' Arctic Region Supercomputing Center (ARSC) [Arctic Region Supercomputing Center (ARSC), 2012], and model outputs are publicly available.

[6] A short description of RAOBS and the fundamental features of HRRR-AK, as well as the climate conditions of study sites, are introduced in section 2. A brief description of converting atmospheric physical parameters into total atmospheric delay and precipitable water vapor (PWV) delay is provided in section 3. In section 4, the experiments focusing on determining the accuracy of using HRRR-AK products for atmospheric signal mitigations in various radar techniques are presented and discussed. The last two sections discuss and summarize the presented work, compare results of this study to other related findings, and draw conclusions on the performance of operational HRRR-AK data for radar signal delay correction.

2. Description of Observations and Study Areas

2.1. Data Descriptions

[7] The HRRR-AK simulations and radiosonde data used in this study cover a time span from June 2010 to September 2011. A brief introduction to the radiosondes used in this study is included in section 2.1.1. The principles of HRRR-AK simulations together with their setup environment and parameterization are provided in section 2.1.2. Five test sites across Alaska have been chosen for this research to cover a wide range of climatic conditions that are routinely encountered in polar and subpolar regions. Their location and climatological details are presented in section 2.1.3.

2.1.1. Radiosonde Observations (RAOBS)

[8] Radiosondes provide in situ observations of the vertical profile of many meteorological variables during their rise through the atmosphere. These variables include atmospheric pressure, temperature, wind speed, and relative humidity [National Weather Service (NWS), 2010]. Typically, radiosondes are released twice a day at 00:00 UTC (15:00 Alaska Standard Time (AKST) in winter, 16:00 Alaska Daylight Time (ADKT) in summer) and 12:00 UTC (03:00 AKST and 04:00 ADKT) [NWS, 2010]. In our research, radiosonde data were retrieved from the University of Wyoming's Department of Atmospheric Science [University of Wyoming, 2012].

[9] The locations of the five radiosonde launch sites used in this study are shown in Figure 1 with their corresponding International Civil Aviation Organization (ICAO) location codes (four-letter code). From north to south, site PABR is located north of Barrow, site PAFA is located southwest of Fairbanks, PANC is to the west of Anchorage, PASN is located in the southeast of St. Paul Island, and PANT is southwest of Annette Island. Two types of radiosondes were used during our studied time span. VIZ II B radiosondes were used at PABR (indicated by a gray dot in Figure 1), while the rest of our test sites (indicated by black dots in Figure 1) were using the VIZ Mark IIs GPS microsonde (VIZ Mark IIs for short in Figure 1) [Morton and Malingowski, 2012]. Both types of radiosondes are very similar in design and are applying the same pressure, temperature, and humidity sensors for recording the atmospheric conditions. Due to this similarity, we will refer to all radiosondes as VIZ radiosondes in the remainder of the paper.

[10] The radiosonde types used in this study have been reported to produce PWV with an accuracy of $\sigma_{\text{RAOBS, PWV}} = 1 - 2$ mm [Niell et al., 2001]. In Arctic regions, the reported accuracy of PWV measurements in Barrow, Alaska is $\sigma_{\text{RAOBS, PWV}} \leq 1$ mm by comparing VIZ observation to GPS products [Mattoli et al., 2007]. Several studies have reported inaccurate records of VIZ radiosondes in the upper

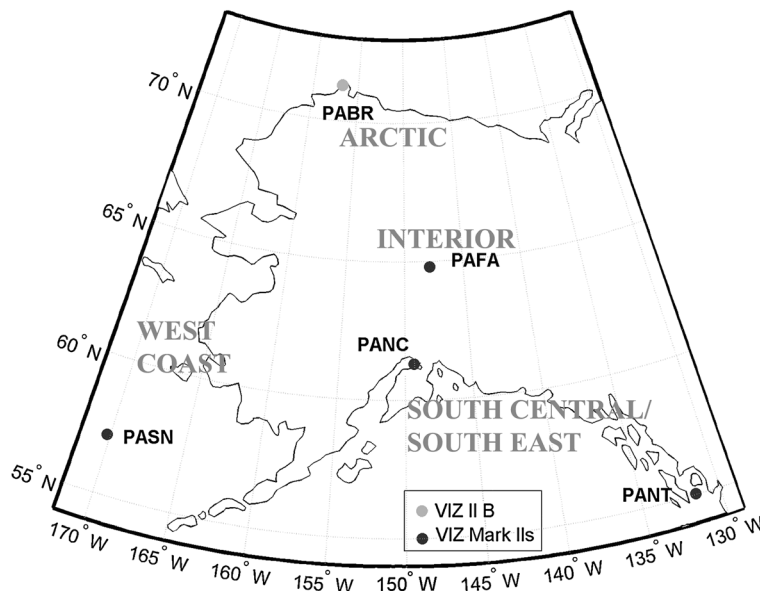


Figure 1. Locations of the radiosonde stations across Alaska that are used in this research. The four-letter codes printed in bold are the ICAO indicators of the observations stations. The gray dot indicates the station using a VIZ II B radiosonde during the study period while black dots represent stations that were using VIZ Mark IIs GPS microsondes. The classified climate regions in Alaska are listed in gray capital letters.

troposphere, when temperatures are extremely cold [Wang and Zhang, 2008]. For InSAR observations, where atmospheric delay signals are primarily dependent on water vapor distributions, measurement errors in the upper troposphere can be largely ignored due to the low proportion of total water vapor in the upper troposphere [Chen *et al.*, 1999]. England *et al.* [1993] have observed distinctive differences in moisture measurements above 8000 m above sea level (asl) among different radiosonde systems. Hence, only the first 8000 m asl of radiosonde data are used for the NWP performance analysis in this research.

2.1.2. HRRR-AK Products and the Weather Research and Forecasting (WRF) Model

[11] The HRRR-AK, which is publicly available for Alaska, <http://weather.arsc.edu/HRRR/>, is initialized with the highly assimilated Rapid Refresh (RAP) data and uses the WRF 3.2 system for 24 h atmospheric condition forecasting with 3 km lateral resolution and 51 vertical layers. The WRF model is a numerical weather prediction and atmospheric simulation system that has been designed for advancing the understanding and prediction of mesoscale weather systems both in research and in operational applications [Skamarock *et al.*, 2008]. WRF belongs to the latest generation mesoscale weather prediction models. Four 24 h HRRR-AK forecasts are produced by ARSC per day providing atmospheric conditions at user defined time steps [ARSC, 2012]. The meteorological initialization data, RAP, are provided by National Oceanic and Atmospheric Administration (NOAA) and is an hourly updated operational weather prediction system covering North America with 13 km lateral resolution and 50 vertical layers [National Oceanic and Atmospheric Administration, 2012]. The 11 km Alaska North American Mesoscale (NAM) model has also been utilized to extend lateral boundary conditions beyond the RAP forecast period. The combination of availability, high lateral and vertical resolution, and rapid temporal refresh rates makes HRRR-AK the ideal data set

for model-based atmospheric correction of radar remote sensing data in an operational setting.

2.1.3. Climate Conditions of Study Areas

[12] The spatial distribution of the radiosonde test sites was chosen to represent a wide range of climate/weather conditions in Arctic and subarctic environments in order to provide a performance assessment of HRRR-AK that are representative for most high-latitude regions. The sites provided a range of meteorological challenges that allowed for testing the robustness of HRRR-AK predictions for several climatic regions.

[13] According to the classification by the Alaska Climate Research Center [Bieniek *et al.*, 2012], Alaska can be generally divided into four climate regions as highlighted in Figure 1 (gray capital letters). These are (i) the Arctic region, (ii) the interior region, (iii) the west coast region, and (iv) the south central/southeast region. The dominating factor that differs among these climate regions is the seasonal change of solar radiation, atmospheric moisture conditions, the local topography, and the presence or absence of nearby ocean bodies [Benson *et al.*, 1983]. Stafford *et al.* [2000] summarized the climate properties of the above mentioned four climate zones. They state that the Arctic climate region, where station PABR is located, can be considered as the coldest and driest with average annual temperatures below 0°C and the majority of precipitation coming from snow [Searby, 1968]. The interior climate region where station PAFA is located is characterized as a highly continental climate of meteorological extremes, with high temperatures ranging from below -40°C in the winter to above +30°C during local AK summer. PASN is located in the Bering Sea, which is considered to be a transitional zone of continental and coastal climates. The two radiosonde stations PANC and PANT are both located in the south central/southeastern climate region that are reported generally wet all year with annual mean temperatures between 0°C and 5°C and are affected by both oceanic and subarctic climates [Peel *et al.*, 2007].

3. Theory of Atmospheric Effects on Radar Remote Sensing and Its Applications

3.1. From Atmospheric Observations to Total Signal Delay

[14] For microwave remote sensing in geodetic applications, the atmosphere is considered an error source that biases measurements of the range between sensor and earth surface. The atmospheric delay L_{los} that is experienced by a microwave signal is equivalent to the integral of refractivity along the signal's line-of-sight (LOS) [Smith and Weintraub, 1953]. Under the assumption of a spatially smooth atmosphere, L_{los} can be calculated from the zenith delay L using the signal's incidence angle θ_{inc} according to $L_{\text{los}} = L \cdot \cos \theta_{\text{inc}}$. As radiosondes measure the vertical profile of atmospheric conditions, vertical delay measurements L are used to assess the performance of HRRR-AK through a direct comparison of $L_{\text{HRRR-AK}}$ and L_{RAOBS} .

[15] The zenith delay L can be further numerically approximated as a function of pressure (P , in hPa), water vapor pressure (e , in hPa) as well as temperature (T , in K) integrated along height h [Smith and Weintraub, 1953], resulting in equation (1), where $k_1 = 77.6\text{K/hPa}$, $k_2 = 23.3\text{K/hPa}$, and $k_3 = 3.75 \times 10^5\text{K}^2/\text{hPa}$ [Smith and Weintraub, 1953; Davis et al., 1985]. The vapor pressure e can be computed from water vapor mixing ratio Q and pressure P [Great Britain. Meteorological Office., 1991], both of which are standard outputs of HRRR-AK and RAOBS.

$$L = 10^{-6} \int \left(\underbrace{k_1 \frac{P}{T}}_{\text{Hydro}} + \underbrace{k_2 \frac{e}{T} + k_3 \frac{e}{T^2}}_{\text{Wet}} \right) dh \quad (1)$$

[16] The first term on the right side of equation (1) is the so-called *hydrostatic* delay (hydro, L_{hydro}), while the second and third terms in equation (1) are the *wet* delay terms (L_{wet}) related to the presence of water vapor. L_{hydro} in the zenith direct can alternatively be calculated from the local gravity g_m in m/s^2 and surface pressure P_s in hPa as shown in equation (2) [Davis et al., 1985; Hanssen, 2001], in which $R_d = 287.053 \text{ [J} \cdot \text{K}^{-1} \text{kg}^{-1}]$. $L_{\text{hydro}} \approx 2.27 \cdot P_s$ in mm with average local gravity $g_m \sim 9.8 \text{ m/s}^2$ in Alaska. Equation (2) utilizes the fact that the vertical atmospheric profiles of pressure P and temperature T are known and stable. This allows us to calculate L_{hydro} without requiring numerical integration, reducing the required computational effort.

$$L_{\text{hydro}} = 10^{-6} \int k_1 \frac{P}{T} dh = 10^{-6} \cdot k_1 \cdot \frac{R_d}{g_m} \cdot P_s \quad (2)$$

[17] An alternative method of calculating the zenith wet delay (ZWD) term L_{wet} in equation (1) is using PWV fields combined with a projection function Π . In equation (3), Π can be considered a dimensionless factor that is mapping PWV into zenith delays. Values for Π were determined from laboratory experiments [Bevis et al., 1992]. Computing L_{wet} via the projection function makes it easier to compare our findings to findings of other researchers that have often analyzed PWV fields from various sources and their potential for atmospheric correction. For instance, when cloud coverage is

not obstructing the atmosphere underneath, PWV fields obtained from multispectral remote sensing, e.g., Moderate Resolution Imaging Spectroradiometer and Medium Resolution Imaging Spectrometer, were used to correct microwave remote sensing signal delays in previous studies [Li et al., 2009; Meyer et al., 2008].

[18] We integrate vapor pressure and temperature in the vertical to obtain PWV and convert PWV to L_{wet} via equation (3). Relying on PWV rather than the vapor and temperature profiles ensures that the methods applied here can be used globally for any NWP or satellite-derived atmospheric information, which often only provide PWV and not profile measurements.

$$L_{\text{wet}} = 10^{-6} \int \left(k_2 \frac{e}{T} + k_3 \frac{e}{T^2} \right) dh = \Pi^{-1} \text{PWV} \quad (3)$$

[19] PWV is derived from predictions of the HRRR-AK system via equation (4) and the performance of these predictions is analyzed through a comparison to RAOBS [Bevis et al., 1992; Hanssen, 2001].

$$\text{PWV} = \frac{1}{\rho_l} \int \left(\frac{e}{R_v \cdot T} \right) \cdot dh \quad (4)$$

[20] The variable ρ_l in equation (4) is the density of liquid water, $R_v = 461.524 \text{ [J} \cdot \text{K}^{-1} \text{kg}^{-1}]$ is the gas constant for water vapor, and vapor pressure e was computed via $e = P \cdot \frac{Q}{0.62197 + Q}$. Therefore, the PWV field is used together with the zenith delay components zenith wet delay L_{wet} (ZWD) and hydrostatic delay L_{hydro} (ZHD) to assess the performance of the reconstructed atmospheric delay field from HRRR-AK.

3.2. Relevant Atmospheric Parameters From a Microwave Remote Sensing Perspective

[21] The atmospheric phase screen that is observed in a SAR interferogram corresponds to the delay difference between two generally uncorrelated states of the atmosphere at two acquisition times [Hanssen, 2001]. It also corresponds to the combination of two different atmospheric signal composites that can be distinguished by their physical origin:

[22] 1. Turbulent mixing, resulting from turbulent convective processes in the atmosphere, creates three-dimensional heterogeneity in the refractivity field.

[23] 2. Vertical stratification is the result of different vertical refractivity profiles at the two SAR acquisitions. Stratification affects mountainous terrain and creates phase signatures that are correlated with topography.

[24] As a double-differencing method, InSAR is sensitive to spatial (meters to kilometers) and temporal (days to years) variations of atmospheric delays. Hence, the atmospheric signals with temporal-spatial correlation lengths comparable to the InSAR sensitivity range can cause relevant errors in InSAR observations. In current advanced radar interferometry techniques, the predominant part of the atmospheric signal in InSAR is caused by the turbulent space-time variation of water vapor in the lower troposphere [Hanssen, 2001]. Therefore, the performance of HRRR-AK for the correction of InSAR data is defined by

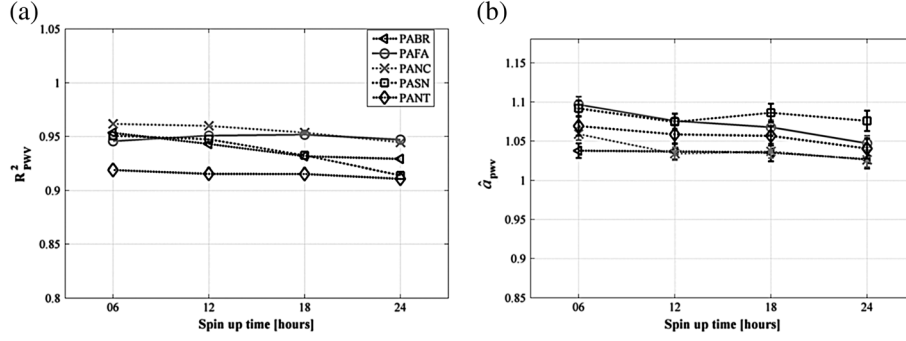


Figure 2. Statistical analysis results of the effect of different HRRR-AK model lead times on the predictability of PWV at each of the test sites. To calculate these statistics, HRRR-AK-derived PWV were compared to radiosonde observations at every station: (a) variation of correlation coefficient R^2_{PWV} ; (b) variation of $\hat{\sigma}_{a,PWV}$ and corresponding $\hat{\sigma}_{a,PWV}$ shown as error bars. Black dashed line with left triangle for PABR; gray bold line with circle for PAFA; gray dashed line with cross for PANC; black dashed line with square for PASN; and black dashed line with black diamond for PANT.

its ability to predict atmospheric water vapor delays, while the quality of hydrostatic delay predictions is of only secondary importance.

[25] Circumstances are different when working with SAR geolocation techniques like tracking methods and absolute ranging. For these methods, the hydrostatic delay plays the leading role in atmospheric interferences, being approximately 10–100 times greater than the wet delay, depending on the weather conditions. For example, the amount of hydrostatic delay can be as much as 2.3 m at sea level, while the wet delay only amounts to about 0.3–0.4 m in some extreme cases [Eineder *et al.*, 2011; Hanssen, 2001].

[26] Hence, the significance of the two terms in equation (1) depends on the radar remote sensing applications. In the following analysis of error budgets, the uncertainty of the predicted wet delay will be used to analyze its effects on SAR interferometry, while the error in the one-way zenith total delay (ZTD) is derived to analyze atmospheric correction of tracking and absolute ranging techniques.

4. Performance Analysis of HRRR-AK Predictions

[27] In order to assess the accuracy of using HRRR-AK in the mitigation of atmospheric delays from radar remote sensing data, experiments were performed where a large number of HRRR-AK simulations were compared to the corresponding atmosphere profiles derived from RAOBS measurements. In the analysis, the HRRR-AK products were grouped according to a set of modeling and environmental parameters to determine the influence of these parameters on HRRR-AK accuracy. These grouping parameters include (i) model lead time, (ii) season of data acquisition, and (iii) sunlight (solar radiation) conditions.

4.1. Applied Mathematical Model for Comparative Analysis

[28] By evaluating the agreement between PWV products from RAOBS and HRRR-AK simulations via linear relationship assumptions, the uncertainty σ_{PWV} of PWV products was determined (see section 4.1.1) and propagated to

determine the wet delay uncertainty $\sigma_{L,wet}$ using equation (5) and assuming a fixed value of Π^{-1} .

$$\sigma_{L,wet} = \Pi^{-1} \sigma_{PWV} \quad (5)$$

[29] Similarly, as will be shown in section 4.1.2, the accuracy $\sigma_{L,hydro}$ of hydrostatic delay predictions was determined using linear regression analysis of HRRR-AK-simulated and RAOBS-observed hydrostatic delays computed via equation (2). Combining the error contributions from the hydrostatic and wet delay together, the error budget of the ZTD σ_L can be expressed following equation (6).

$$\sigma_L = \left(\sigma_{L,wet}^2 + \sigma_{L,hydro}^2 \right)^{1/2} = \left[\left(\Pi^{-1} \sigma_{PWV} \right)^2 + \sigma_{L,hydro}^2 \right]^{1/2} \quad (6)$$

[30] While equation (6) describes atmospheric delay errors in a single SAR acquisition, the differential delay information in an interferogram can be calculated from equation (6) via

$$\sigma_{L,ifg} = \sqrt{2} \sigma_L \quad (7)$$

[31] To be able to compare RAOBS-observed and HRRR-AK simulated atmospheric data, the vertical RAOBS profiles were additionally resampled to match the vertical levels of the HRRR-AK model using linear interpolation methods.

4.1.1. Assessment of the Accuracy of Precipitable Water Vapor Predictions

[32] Both RAOBS and HRRR-AK delays were integrated along the vertical to provide pairs of integrated PWV products. For comparison and statistical analysis, a linear relationship between HRRR-AK-simulated ($PWV_{HRRR-AK}$) and radiosonde-observed (PWV_{RAOBS}) PWV products was assumed and applied. Using linear regression models for such analysis has been suggested in previous studies [Li *et al.*, 2006b; Niell *et al.*, 2001], where free regression models were used to describe and analyze the relationship of radiosonde observations and multispectral remote sensing PWV measurements. In contrast to these studies, we applied a slightly modified approach that recognizes the physical

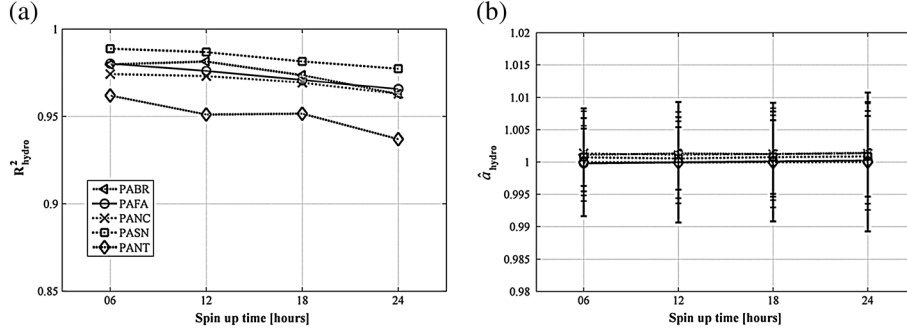


Figure 3. Statistical analysis results of the effect of different HRRR-AK model lead times on the accuracy of hydrostatic delay predictions at the five test sites: (a) variation of correlation coefficient R^2_{hydro} ; (b) variation of \hat{a}_{hydro} and corresponding $\hat{\sigma}_{\hat{a}_{\text{hydro}}}$ shown as error bars. Black dashed line with left triangle for PABR; gray bold line with circle for PAFA; gray dashed line with cross for PANC; black dashed line with square for PASN; and black dashed line with black diamond for PANT.

properties of PWV measurements that prohibit negative values of PWV. Hence, in our analysis, the linear regression lines are forced through $(0, 0)$ to guarantee physically meaningful results (equation (8)).

$$\text{PWV}_{\text{HRRR-AK}} = a \cdot \text{PWV}_{\text{RAOBS}} \quad (8)$$

[33] The best fitting regression model was found using a least squares fitting approach, where the radiosonde measurements were assumed error free and the best fitting regression slope \hat{a} is found from equation (9)

$$\hat{a} = \arg \min_a \left(\|\text{PWV}_{\text{HRRR-AK}} - a \cdot \text{PWV}_{\text{RAOBS}}\|^2 \right) \quad (9)$$

[34] Moreover, we apply robust regression techniques where outliers among the RAOBS are identified and discarded to provide unbiased estimates of HRRR-AK performance. Most outliers were caused by instrument failures in the upper troposphere. In a preprocessing step, we also discard radiosonde records with large data gaps below 8000 m.

[35] In addition to the estimated slope \hat{a} , a set of statistical parameters that describe the quality of the fitting model are derived. The coefficient of determination R^2 is used in this study to determine the goodness of fit between HRRR-AK and RAOBS data. It is calculated according to equation (10).

$$R^2 = 1 - \frac{\sum_{i=1}^N (\text{PWV}_{\text{HRRR-AK},i} - f_i)^2}{\sum_{i=1}^N (\text{PWV}_{\text{HRRR-AK},i} - \mu(\text{PWV}_{\text{HRRR-AK}}))^2} \quad (10)$$

where N is the total number of data pairs, $f_i = \hat{a} \cdot \text{PWV}_{\text{RAOBS},i}$, and $\mu(\cdot)$ is the arithmetic mean. The standard deviation $\hat{\sigma}_{\hat{a}}$ of the slope estimate is also analyzed. $\hat{\sigma}_{\hat{a}}$ expresses how well the slope is defined and additionally allows to statistically compare the slope estimates at different locations or derived from different parameter settings in NWP simulations.

[36] A third parameter computed is the root-mean-square (RMS) of the residuals σ_{res} (see equation (11)). σ_{res} is used to express the uncertainty of the PWV products due to random noise. Here we assume that nonlinear systematic errors of RAOBS measurements or HRRR-AK model can be

Table 1. Statistical Analysis of One Say Zenith Delay for Several Test Sites in Alaska at 6 h and 24 h Model Lead Time Settings^a

Site Name	Lead Time (hour)	PWV ^b		Wet Delay	Hydrostatic Delay		Total Delay	PWV Range (mm) Min–Max (mean) ^d
		\hat{a}_{PWV}	σ_{PWV} (mm)	$\sigma_{L,\text{wet}}$ (mm) ^c	\hat{a}_{hydro}	$\sigma_{L,\text{hydro}}$ (mm)	σ_L (mm)	
PABR	6	1.04	1.31	8.48	1.00	3.14	9.04	1.06–27.53 (8.58)
	24	1.03	1.62	10.55	1.00	4.43	11.44	
PAFA	6	1.10	1.90	12.38	1.00	3.65	12.90	1.09–30.88 (12.12)
	24	1.05	1.80	11.71	1.00	4.72	12.63	
PANC	6	1.06	1.47	9.56	1.00	4.09	10.40	0.81–33.74 (12.83)
	24	1.03	1.72	11.19	1.00	4.88	12.20	
PASN	6	1.09	1.62	10.53	1.00	3.19	11.00	1.72–34.73 (11.93)
	24	1.08	2.08	13.51	1.00	4.63	14.29	
PANT	6	1.07	1.91	12.41	$\hat{a}_{\text{PWV}} 1.00$	4.23	13.11	1.50–37.03 (14.57)
	24	1.04	1.99	12.95	1.00	5.36	14.02	
All	6	/	1.66	10.77	/	3.69	11.39	/
	24	/	1.85	12.00	/	4.81	12.93	/

^aStatistics are relative to a linear best fitting regression model.

^bThe first row of the table denotes the main columns. For example, column 3 is presenting PWV statistics while σ_{PWV} will be referred as subcolumn of column 3 (the same as the following tables).

^c $\sigma_{L,\text{wet}}$ uncertainty of one-way zenith wet delay was calculated via equation (5).

^dPWV conditions computed from radiosonde observations (the same as the following tables).

Table 2. RMS (Bias) of Difference (HRRR-AK Minus RAOBS) at 6 h and 24 h Model Lead Time Settings^a

	PABR	PAFA	PANC	PASN	PANT	All	All ZWD	All ZHD	All ZTD
6 h	1.36 (0.31)	2.35 (1.34)	1.71 (0.87)	2.05 (1.19)	2.21 (1.18)	1.97 (0.98)	12.79 (6.37)	4.19 (1.34)	13.46 (7.71)
24 h	1.65 (0.25)	1.92 (0.74)	1.76 (0.46)	2.32 (1.03)	2.09 (0.69)	1.96 (0.63)	12.72 (4.10)	5.29 (1.78)	13.78 (5.88)

^aThe rows show RMS (bias) values of PWV for every analyzed test site, overall PWV RMS (bias) for all test sites, overall RMS (bias) of delay components (unit, mm) (the same as Tables 5 and 8).

ignored, such that σ_{res} can be considered as the error bound for the evaluated parameters, $\sigma_{\text{PWV}} \hat{\sigma}_{\text{res}}$.

$$\sigma_{\text{res}} = \sqrt{\frac{\sum_i^N (\text{PWV}_{\text{HRRR-AK},i} - f_i)^2}{N-1}} \quad (11)$$

[37] The above outlined parameters only provide a full description of HRRR-AK performance if (1) the relationship between RAOBS and HRRR-AK parameters is linear and (2) if forcing our regression lines through zero does not result in nonstationary residuals. To avoid a misrepresentation of model performance, the RMS (σ_{RMS}) and bias (μ_{RMS}) of the *point-by-point differences* between RAOBS and HRRR-AK observations are calculated in addition to the above parameters. These additional parameters are free of linearity assumptions and allow for identifying nonstationary biases in the model predictions.

4.1.2. Assessment of the Accuracy of Hydrostatic Delay Predictions

[38] After resampling to identical vertical sampling locations, the pressure information of the bottommost layer of both HRRR-AK and RAOBS is extracted and used as surface pressure to derive the hydrostatic delay from HRRR-AK ($\text{Hydro}_{\text{HRRR-AK}}$) and RAOBS ($\text{Hydro}_{\text{RAOBS}}$) via equation (2). A linear relationship, identical to the one described by equation (8), is assumed and applied for analyzing the quality of hydrostatic delay predictions ($\text{PWV}_{\text{HRRR-AK}}$ and $\text{PWV}_{\text{RAOBS}}$ are replaced with $\text{Hydro}_{\text{HRRR-AK}}$ and $\text{Hydro}_{\text{RAOBS}}$, respectively, in equation (8)). Again, several parameters are used to describe the quality of the regression model including computing the estimated slope \hat{a} coefficient and its uncertainty $\hat{\sigma}_a$, R^2 , and σ_{res} (used as the uncertainty of HRRR-AK hydrostatic delay products, assuming $\sigma_{L,\text{hydro}} = \sigma_{\text{res}}$), as well as the RMS (σ_{RMS}) and the bias (μ_{RMS}) of the point-by-point differences.

4.2. Results of Experiments

4.2.1. Performance of HRRR-AK as a Function of Model Lead Time.

[39] Several HRRR-AK model runs with model lead times of 6 h, 12 h, 18 h, and 24 h were computed and compared to RAOBS observations. Model lead time is the period from the

model start time to the time stamp for which the model output is retrieved. Weather models need enough time to “spin-up” from an initial state—often derived by interpolating from coarser to finer domains—to one in which the meteorology has fully developed within the finer, computational domain [Skamarock, 2004]. For example, typical model runs start with no precipitation and need some spin-up time to introduce it in a stable way. Choosing the appropriate model lead time is critical: If the lead time is chosen too short, the model may not have reached steady state, reducing the quality of the model output. Similarly, if the model lead time is selected too long, the quality of the model output may decrease as errors accumulated in capturing the large scale structure [Wang et al., 2011]. In order to determine if the optimal model lead time depends on the local climatic conditions, the data were analyzed for each of our test sites separately. With this setup, more than 600 HRRR-AK/RAOBS combinations were available for each experiment, providing an excellent data base for statistical analysis.

[40] Figure 2 shows the influence of model lead time on PWV estimates by plotting correlation coefficient R_{PWV}^2 (Figure 2a) and estimated slope coefficient \hat{a}_{PWV} together with $\hat{\sigma}_{\hat{a}_{\text{PWV}}}$ (Figure 2b). In Figure 2a, a value close to one represents perfect linearity between HRRR-AK and RAOBS-derived total PWV. The overall R_{PWV}^2 values at all five subtest sites are larger than 0.9 for all forecast period, indicating a good agreement between PWV products from HRRR-AK and radiosonde observations. While the agreement to a linear relationship is good in all cases, the estimated slope values \hat{a} show some variation with model lead time and location (see Figure 2b). From an analysis of Figure 2b, we can conclude that (i) the value of \hat{a}_{PWV} is always larger than 1 indicating that HRRR-AK is overestimating water vapor content relative to RAOBS measurements; (ii) for all five stations, we observed a slight, yet statistically insignificant, reduction of \hat{a}_{PWV} when increasing the forecast simulation length, which indicates that the HRRR-AK is slowly getting drier. The error bars in Figure 2b indicate the magnitude of $\hat{\sigma}_a$, which is changing very little with model lead time.

[41] The study shows that overall ability of HRRR-AK to predict the water vapor field is not significantly degrading with increasing forecast length. The very stable R_{PWV}^2 and

Table 3. Statistical Analysis of One-Way Zenith Delay of Summer Cases at 12 h Model Lead Time Setting

Site Name	PWV			Wet Delay		Hydrostatic Delay			Total Delay	PWV Range (mm) Min–Max (mean)
	\hat{a}_{PWV}	R_{PWV}^2	σ_{PWV} (mm)	$\sigma_{L,\text{wet}}$ (mm)	\hat{a}_{hydro}	R_{hydro}^2	$\sigma_{L,\text{hydro}}$ (mm)	σ_L (mm)		
PABR	1.09	0.75	2.76	17.91	1.00	0.97	2.99	18.16	3.04–27.53 (12.94)	
PAFA	1.08	0.78	2.36	15.32	1.00	0.96	3.43	15.70	3.77–30.88 (17.62)	
PANC	1.04	0.85	1.84	11.96	1.00	0.97	3.54	12.47	4.94–33.10 (18.28)	
PASN	1.08	0.85	2.29	14.89	1.00	0.98	3.29	15.25	6.00–34.73 (16.65)	
PANT	1.06	0.78	2.45	15.91	1.00	0.92	4.27	16.47	6.61–37.55 (18.67)	
All	\	\	2.35	15.30	\	\	3.35	15.70	\	

Table 4. Statistical Analysis of One-Way Zenith Delay of Winter Cases at 12 h Model Lead Time Setting

Site Name	PWV			Wet Delay	Hydrostatic Delay			Total Delay	PWV Range (mm) Min–Max (mean)
	\hat{a}_{PWV}	R^2_{PWV}	σ_{PWV} (mm)	$\sigma_{L,wet}$ (mm)	\hat{a}_{hydro}	R^2_{hydro}	$\sigma_{L,hydro}$ (mm)	σ_L (mm)	
PABR	0.98	0.95	0.57	3.71	1.00	0.99	2.90	4.71	1.06–15.11 (4.21)
PAFA	1.08	0.92	0.94	6.13	1.00	0.99	4.01	7.33	1.10–18.20 (4.94)
PANC	1.04	0.91	1.05	6.84	1.00	0.98	4.50	8.19	0.81–22.59 (6.31)
PASN	1.05	0.86	1.31	8.54	1.00	0.99	3.77	9.33	1.69–23.86 (6.63)
PANT	1.06	0.90	1.41	9.14	1.00	0.97	4.70	10.27	1.50–21.20 (9.44)
All	\	\	1.09	7.10	\	\	4.02	8.16	\

\hat{a}_{PWV} (Figure 2) parameters show that the model does not develop a bias with time.

[42] The same linear regression procedures were also applied to assess the quality of hydrostatic delay products. The estimated R^2_{hydro} and slope coefficients \hat{a}_{hydro} of hydrostatic delay products as well as corresponding uncertainties $\hat{\sigma}_{\hat{a}_{hydro}}$ are shown in Figure 3. In Figure 3a, the R^2_{hydro} values calculated from five test sites are larger than 0.93 for all model lead times and locations, indicating an excellent linear relationship between RAOBS-observed and HRRR-AK-simulated hydrostatic delays. In Figure 3b, \hat{a}_{hydro} values are shown to be statistically identical to 1 and statistically independent on model lead time (tested at the 95% confidence level).

[43] More details on the derived HRRR-AK prediction performance are summarized in Table 1, showing the statistical parameters for all five stations at 6 h and 24 h forecast period. In addition to the station-by-station analysis, a sixth segment is added at the bottom of the table that shows the average HRRR-AK performance across *all* test sites. σ_{PWV} in Table 1 is calculated from the RMS of the residuals σ_{res} assuming a linear regression model (see equation (11)). The wet delay accuracy $\sigma_{L,wet}$ in Table 1 was calculated based on equation (5). $\sigma_{L,wet}$ is less than 13.00 mm, when using products at 6 h forecast period, and only increases slightly when increasing model lead time to 24 h. The statistics of the hydrostatic delay (two subcolumns in column 5 Table 1) show that the uncertainty of one-way hydrostatic delay predictions $\sigma_{L,hydro}$ is always less than 5.40 mm and shows only a little dependence on model lead time. Considering that the hydrostatic delay could be as large as 2.30 m at sea level, these numbers show that L_{hydro} can be estimated with a relative error of 0.3% from HRRR-AK products in high-latitude regions.

[44] As shown by column 6 in Table 1, the variation of total atmospheric delay uncertainty σ_L with forecast period

time is small. Together with $\sigma_{L,wet}$ and $\sigma_{L,hydro}$, the overall σ_L determined via equation (6) at 6 h model lead time ranges from $9.04 \text{ mm} \leq \sigma_L \leq 13.11 \text{ mm}$. For a 24 h forecast duration, σ_L is very similar with $11.44 \text{ mm} \leq \sigma_L \leq 14.29 \text{ mm}$. Comparing column 4 and 6 in Table 1, the major source of error in the HRRR-AK simulations is the model’s relatively limited handling of PWV.

[45] The wet and total delay performance of HRRR-AK shows dependence on test site with dryer climates showing better performance than more humid climates (see last column of Table 1 for the range of atmospheric moisture across test sites). This is a direct consequence of the model’s limited performance in predicting PWV and is, as such, in line with expectations.

[46] To supplement the information in Table 1, which represents the deviation of HRRR-AK from a linear regression model, Table 2 adds the model-free point-by-point statistics for further analysis. As σ_L is almost entirely driven by errors in PWV, only the point-by-point statistics ($\sigma_{wet,RMS}$ and $\mu_{wet,RMS}$) of the wet delay are shown. The results in Table 2 show a significant reduction of model bias from 6 h to 24 h model lead time, indicating that the model is getting drier when the model lead time is increased. This is consistent with the results based on regression analysis, for which a decrease in slope with increasing lead time was reported. RMS values reported in Table 2 are slightly larger than their regression-based counterparts in Table 1. This is expected as they include the full bias between observations and model while the regression-based variables only include residual biases after a best fitting regression line was removed. Hence, regression-based and regression-free error analyses are consistent.

[47] Taken together, when applying HRRR-AK to compensate for atmospheric effects in radar signals across the Alaska region, absolute geodetic range measurements can be obtained with an accuracy of better than 14.3 mm (max

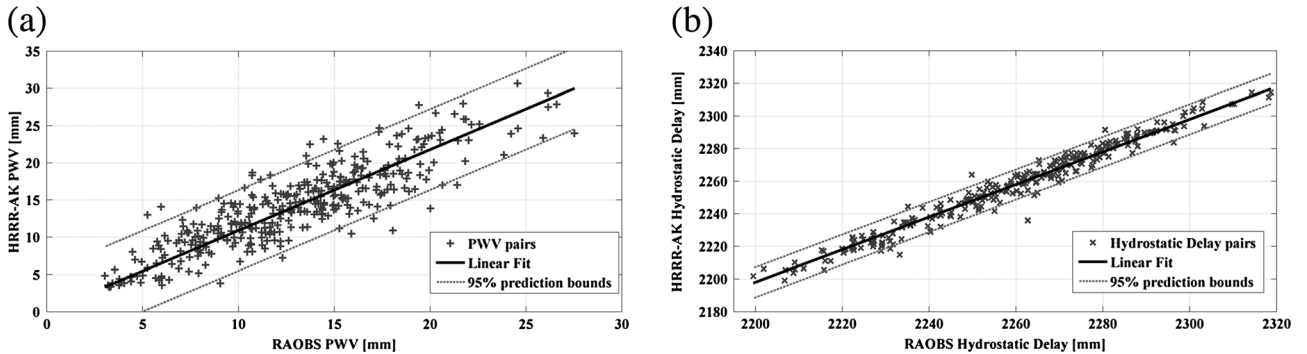


Figure 4. Examples of linear regression of HRRR-AK versus RAOBS data for PWV and hydrostatic delay. (a) Linear regression of PWV data pairs at station PABR over summer period, (b) linear regression of hydrostatic delay data pairs at station PANT over winter period.

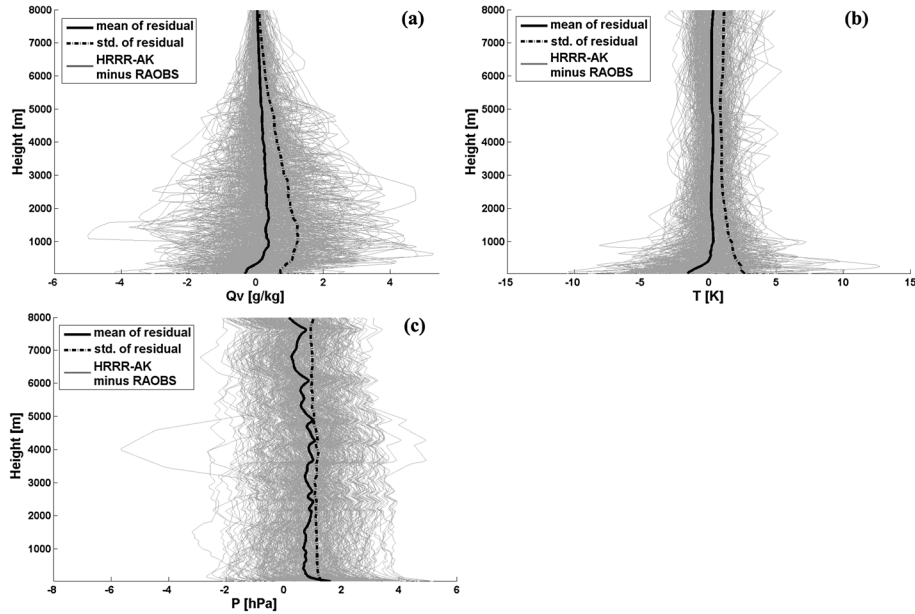


Figure 5. Examples of vertical profiles of atmospheric parameters extracted from PABR summertime data pairs. (a) Vertical profile of Q_v ; (b) Vertical profile of T ; and (c) Vertical profile of P . Gray thin lines show the residuals of HRRR-AK-simulated atmospheric parameters minus RAOBS corresponding records. Black solid lines are computed from the mean of residuals at corresponding height and black dashed lines are the standard deviation of residuals.

σ_L in Table 1, PASN 24 h products). Assuming a spatially stationary process, we can furthermore conclude that for the studied climate conditions InSAR atmospheric delay errors can be corrected with a residual error of better than $\sigma_{L,ifg} = \sqrt{2} \cdot \sigma_L = 20.2$ mm. Most of the residual atmospheric errors are due to the model’s limited ability to predict $\sigma_{L,wet}$. This finding is in good agreement with other studies where NWP predictions were compared to PWV maps from InSAR and spaceborne multispectral scanners [Liu and Hanssen, 2009].

[48] Due to the limited dependence on model lead time, only the HRRR-AK 12 h products paired with corresponding RAOBS will be used for evaluating and analyzing seasonal influences and effects from sunlight condition on HRRR-AK performance.

4.2.2. Statistics of HRRR-AK Products With Seasonal Effects

[49] The quality of HRRR-AK products was also evaluated according to the seasonal dependence. Considering the special climate conditions of high-latitude areas, where both spring and autumn are very short, we divided the annual climate into two parts, (1) the winter season with snow from November to May, and (2) the summer season from June to October based on a study of snowmelt dates in Barrow, AK [Stone et al., 2002].

[50] For performance analysis, regression models were calculated from HRRR-AK/RAOBS comparisons for all five

stations and for local AK winter and summer periods separately. In addition to the station-by-station analysis, also the average seasonal dependence of HRRR-AK across all test sites was calculated. The detailed statistics of the local AK summer analyses are listed in Table 3 and local AK winter cases are shown in Table 4. In both tables, column 2 and 3 address PWV and wet delays, while column 4 analyzes hydrostatic delay, and the total delays as well as the corresponding PWV ranges at the study sites are shown in last two columns.

[51] In Table 3, the coefficient of determination R_{PWV}^2 of PWV regressions is larger than 0.75 for all five local AK summer cases. This indicates that the linear model of equation (8) explains at least three quarter of variance in all the data pairs. σ_{PWV} in the local AK summer time varies strongly throughout our five test sites with the maximum of $\sigma_{PWV} \leq 2.76$ mm observed for PABR, corresponding to $\sigma_{L,wet} \leq 17.91$ mm. Site PANC presents the best PWV performance of all local AK summer time cases, producing smallest σ_{PWV} and $\sigma_{L,wet}$. Considering the relative high humidity condition in this region [Stafford et al., 2000], PANC indicates the highest relative PWV accuracy of all analyzed HRRR-AK products. The regression of hydrostatic delay in Table 3 shows excellent fit with R_{hydro}^2 larger than 0.92 and $\sigma_{L,hydro}$ smaller than 4.27 mm. By integrating the uncertainty of wet delay and hydrostatic delay together via equation (6), the total delay uncertainty σ_L for all local

Table 5. RMS (Bias) of Difference for Winter and Summertime Acquisitions (HRRR-AK 12 h Products Minus RAOBS)

	PABR	PAFA	PANC	PASN	PANT	All	All ZWD	All ZHD	All ZTD
Winter	0.58 (−0.09)	1.04 (0.40)	1.10 (0.33)	1.37 (0.44)	1.53 (0.60)	1.16 (0.33)	7.57 (2.16)	4.38 (0.16)	8.74 (2.33)
Summer	3.01 (1.35)	2.78 (1.66)	1.97 (0.85)	2.69 ($\sigma_{L,hydro}$ 1.47)	2.70 (1.30)	2.65 (1.33)	17.25 (8.61)	4.34 (2.30)	17.79 (10.92)

Table 6. Performance Analyzes of Daylight Effects to Simulation, 12:00 UTC-Nighttime

Site Name	PWV			Wet Delay	Hydrostatic Delay			Total Delay	PWV Range (mm) Min–Max (mean)
	\hat{a}_{PWV}	R^2_{PWV}	σ_{PWV} (mm)	$\sigma_{L,\text{wet}}$ (mm)	\hat{a}_{hydro}	R^2_{hydro}	$\sigma_{L,\text{hydro}}$ (mm)	σ_L (mm)	
PANC	1.01	0.97	1.39	9.04	1.00	0.97	4.23	9.98	0.81–32.50 (13.29)
PASN	1.05	0.96	1.57	10.18	1.00	0.99	3.81	10.87	1.85–33.24 (12.45)
PANT	1.02	0.93	1.82	11.80	1.00	0.94	5.13	12.87	1.88–37.55 (15.08)
All	\	\	1.59	10.36	\	\	4.42	11.26	\

summer cases is ranging between 12.47 mm and 18.16 mm, which is worse than the all year average performance of the model shown in Table 1.

[52] Table 4 shows the results of the HRRR-AK/RAOBS comparison during local AK winter conditions. Due to the dryer conditions during the winter months, the HRRR-AK-simulated PWV products have smaller absolute errors with $0.57 \text{ mm} \leq \sigma_{\text{PWV}} \leq 1.41 \text{ mm}$, corresponding to $3.17 \text{ mm} \leq \sigma_{L,\text{wet}} \leq 9.14 \text{ mm}$. The simulated hydrostatic delay is again of high accuracy with $\sigma_{L,\text{hydro}} \leq 4.70 \text{ mm}$, leading to an estimated σ_L of less than 10.3 mm.

[53] Differences between local AK wintertime and summertime performance are pronounced in particular for the predicted wet delay component. Model overestimation (expressed by $\hat{a}_{\text{PWV}} > 1$) at sites PABR and PASN, as well as the residual signal variance σ_{PWV} at all test sites are larger during the local AK summer, where more water vapor is present in the atmosphere [Picon *et al.*, 2003].

[54] The highest σ_{PWV} is observed in the local AK summertime for station PABR, whose water vapor field regression is shown in Figure 4a. It can be seen that, while significant noise exists about the regression line, the relationship between RAOBS and HRRR-AK still maintains a good linear correlation. Also, only a few outliers (points outside 95% prediction bound) are present even in this worst case scenario.

[55] To further investigate the cause for the limited PWV estimation performance of HRRR-AK, the atmospheric parameters that contribute to the wet delay were evaluated, including vapor mixing ratio Q_v , temperature T , and pressure P (cf. equation (4)). The vertical profiles of Q_v , T , and P at PABR for local AK summer cases are plotted in Figures 5a–5c, respectively. Figure 5a shows the residual of Q_v after subtraction of RAOBS measurements from HRRR-AK predictions for a large number of observation epochs (gray solid thin lines). The mean value profile of these Q_v residuals (solid black line in Figure 5a) indicates that HRRR-AK is underestimating RAOBS-observed Q_v near the ground and slightly overestimates Q_v in higher altitudes. The standard deviation profile of the Q_v residuals (dashed black line) shows large noise levels in the lower troposphere where stronger differences between HRRR-AK predictions and RAOBS can be observed. As the standard deviation of the

residuals is larger than the mean for all height levels, no significant biases can be shown for HRRR-AK-derived Q_v data. In Figure 5b, vertical profiles of atmospheric temperature T are shown. The mean value profile shows a noticeable but statistically insignificant underestimation of T close to the ground and unbiased performance at higher altitudes. Pressure profiles (Figure 5c) demonstrate an overestimation across many height levels. Especially at near ground level, the residual mean is slightly larger than the residual standard deviation, suggesting a statistically significant overestimation. It is likely that the overestimation of Q_v and P led to estimated slope value of $\hat{a}_{\text{PWV}} > 1$ and increases the uncertainty of PWV products of HRRR-AK (Table 3, column 2 and 3).

[56] In contrast to the wet delay predictions, the hydrostatic delay data show no dependence on season. Regression slopes as well as residual delay variance $\sigma_{L,\text{hydro}}$ are statistically identical for local AK summer and winter. $\sigma_{L,\text{hydro}}$ is the largest for local winter data pairs at station PANT (shown in Figure 4b). The tight grouping about the best fitting regression line (see Figure 4b) shows the excellent performance of HRRR-AK in predicting hydrostatic delay.

[57] Comparing term σ_L in Tables 3 and 4, an evident seasonal dependence can be observed. This dependence comes from the $\sigma_{L,\text{wet}}$ in local AK summer cases being approximately 1.5–2 times larger than in local AK winter. Overall, the one-way total delays in zenith direction among the five test sites can be predicted with accuracy better than 10.5 mm in the local AK wintertime and better than 18.2 mm in the local AK summer periods.

[58] The point-by-point statistics are listed in Table 5. Comparing the average total delay accuracy in summer (15.70 mm; last row Table 3) and in winter (8.16 mm; last row Table 4) with statistics in the last column of Table 5 (17.79 mm in summer and 8.74 in winter) shows consistency between the regression-based and the regression-free statistics.

[59] Note that regression slopes estimated for hydrostatic delay are always statistically identical to 1 (95% confidence limit), while the slopes for wet delays \hat{a}_{PWV} are all statistically larger than 1 (with exception of wintertime data for station PABR). Li *et al.* [2006b] reported similar overestimating behavior when comparing PWV products from optical remote sensing to RAOBS observations and GPS products comparing

Table 7. Performance Analyzes of Daylight Effects to Simulation, 00:00 UTC-Daytime

Site Name	PWV			Wet Delay	Hydrostatic Delay			Total Delay	PWV Range (mm) Min–Max (mean)
	\hat{a}_{pwv}	R^2_{pwv}	σ_{pwv} (mm)	$\sigma_{L,\text{wet}}$ (mm)	\hat{a}_{hydro}	R^2_{hydro}	$\sigma_{L,\text{hydro}}$ (mm)	σ_L (mm)	
PANC	1.06	0.96	1.50	9.74	1.00	0.98	4.03	10.54	1.05–33.10 (12.35)
PASN	1.11	0.94	1.75	11.40	1.00	0.99	3.33	11.87	1.69–34.73 (11.35)
PANT	1.10	0.91	2.05	13.35	1.00	0.96	4.40	14.06	1.50–37.05 (14.15)
All	\	\	1.78	11.56	\	\	3.96	12.22	\

Table 8. RMS (Bias) of Difference in Different Daylight Condition Cases (HRRR-AK 12 h Products Minus RAOBS)

	PANC	PASN	PANT	All	All ZWD	All ZHD	All ZTD
Daytime	1.74(0.92)	2.28(1.35)	2.54(1.47)	2.15(1.10)	14.01(7.15)	4.21(0.68)	14.97(7.83)
Nighttime	1.39(0.20)	1.70(0.65)	1.85(0.49)	1.66(0.49)	10.80(3.21)	4.84(1.73)	11.80(4.94)

RAOBS by *Mattioli et al.* [2007]. This may indicate that the differences between HRRR-AK and RAOBS data are caused by the RAOBS observations rather than the atmospheric model. However, further experiments are needed to confirm this conclusion.

4.2.3. Performance of HRRR-AK Products as a Function of Time of Day.

[60] *Kuo and Sun* [1976] concluded that the atmosphere is usually stable at all vertical levels during the night, while during daytime, shortwave solar radiation is leading to unstable atmospheric conditions. This diurnal variation may cause a variation of HRRR-AK performance with time of day.

[61] Additionally, most microwave remote sensing systems operate in sun synchronous orbits with mean local times in descending mode of either around 10:00 A.M. (10:00 P.M. for ascending), e.g., Environmental Satellite (ENVISAT), or around ~6:00 A.M. (6:00 P.M. for ascending), e.g., for TerraSAR-X and Cosmo-SkyMed. Hence, a study of daylight effects on the performance of HRRR-AK is useful to predetermine achievable atmospheric correction accuracies for microwave remote sensing systems with different acquisition modes.

[62] For this study, the data stack has been grouped into two categories: (i) nighttime data pairs (12:00 UTC, 03:00 AKST and (ii) daytime data pairs (00:00 UTC, 15:00 AKST). Due to the effects of the midnight sun on regions above the Arctic Circle (latitude higher than 66.56 degree in north hemisphere), both test site PABR with latitude 71.3° and PAFA at latitude 65° North are suffering difficulty to classify data pairs acquired at different daylight condition. Hence, to keep the simplicity of grouping the RAOBS and HRRR-AK data pairs from different sunlight condition, only the lower latitude stations, including PANC, PASN, and PANT, were selected for this study, for which variations of sunrise and sunset times are less. A 12 h model lead time was used, and the statistics of PWV and radar signal delay products were computed and listed in Tables 6 (nighttime cases) and 7 (daytime cases).

[63] Both nighttime and daytime data show good linear correlation behavior with R_{PWV}^2 and R_{hydro}^2 values larger than 0.9. There is no statistically significant effect of sunlight on the uncertainty of one-way total delay σ_L measurements (95% confidence level). While there are no effects on the total delay regression parameters, significant effects on the estimated PWV regression slopes \hat{a}_{PWV} and minor effects on the estimation uncertainty of wet delays $\sigma_{L,wet}$ can be observed. Slopes \hat{a}_{PWV} are larger and $\sigma_{L,wet}$ increases during daytime. In contrast to the wet delay components, the computed $\sigma_{L,hydro}$ is slightly smaller for the daytime cases.

[64] The point-by-point statistics of daylight effects are listed in Table 8. It shows that, on average, biases of the ZWD are about 4 mm higher during daytime than at night while ZHD biases are similar for day and nighttime conditions. This leads to ZTD daytime biases that exceed nighttime biases by about 3 mm. RMS values show very similar behavior, with daytime RMS values exceeding nighttime values by

4mm and 3mm for ZWD and ZTD, respectively. The results from regression-based and point-by-point analyses are again consistent, indicating that the regression approach did not introduce errors in our performance parameters.

5. Discussion

5.1. Comparison With Other NWP Products in Delay-Related Components Prediction

[65] To investigate the performance of HRRR-AK relative to other NWP systems, we conducted a literature research of studies that assessed the performance of NWPs for signal delay correction. Four major global meteorological data were used in the identified studies (listed in column one in Table 9), including (1) reanalysis products from the European Centre for Medium-Range Weather Forecasts (ECMWF) (e.g., ERA-Interim reanalysis products from ECMWF) [*Cong et al.*, 2012], (2) the National Centers for Environmental Prediction-National Center for Atmospheric Research (NCEP-NCAR) Reanalysis I (NCEP-I), (3) the NCEP-Department of Energy reanalysis II (NCEP-II), and (4) initial boundary conditions generated from the Meteorological Assimilation Data Ingest Systems (MADIS) via the assimilation system, e.g., Local Analysis and Prediction System (LAPS) [*Foster et al.*, 2013].

[66] In some of the studies, the meteorological data were feed into various NWP models as initial boundary condition to produce “customized” simulations, e.g., studies conducted by *Pacione et al.*[2001], *Behrend et al.*[2002], and *Foster et al.* [2013] as well as HRRR-AK (Table 9). The other identified case studies, however, focused on the performance assessment of global meteorological data without customized refinements, e.g., the studies from *Bock and Nuret* [2009] and *Cong et al.* [2012]. The main NWP model that was used in these studies is the National Center for Atmospheric Research-Penn State Mesoscale Model Version 5 (MM5).

[67] A comparison of HRRR-AK with other systems is complicated by the fact that previous studies used very inconsistent analysis parameters. As summarized in column 1 of Table 9, a wide range of parameters was used to analyze NWP performance including PWV, ZWD, and ZTD values. Also, for performance analysis, the studied NWPs were compared to a range of reference data including GPS products and Very Long Baseline Interferometry (VLBI) (see column 3 of Table 9 for information on applied reference data). Moreover, two types of statistics are listed in column 5 of Table 9 including the standard deviation of difference between model and reference data marked by superscript “c”, while the rest were computed using the root-mean-square of differences. Additionally, the data time span of every study is listed in column 6 of Table 9 to help in understanding the representativeness of statistics from different studies.

[68] To facilitate a comparison of our results to these published data, also the findings from our study are listed in Table 9 (see last three rows). We are listing the winter-summer statistics using 12 h model lead times as well as the

Table 9. Statistics (Bias and RMS Difference or Standard Deviation of Difference) Adapted From Previous Studies of Different NWP Products in Predicting Delay-Related Parameters, Including PWV, ZWD, and ZTD^a

Initial Data/Study Field	NWP Model	Reference Data	Bias	Standard Deviation/RMS	Time Span	Literature Source
ECMWF/PWV	MM5	GPS	4.0–5.6	2.3–6.7 ^d	July–October 1999	Table 5, <i>Pacione et al.</i> [2001]
ECMWF/PWV ^b	\	GPS	0	3.4 ^d	2005–2007	Table 4, <i>Bock and Nuret</i> [2009]
NCEP-I/PWV ^b	\	GPS	0.7	5.4 ^d	2005–2007	Table 4, <i>Bock and Nuret</i> [2009]
NCEP-II/PWV ^b	\	GPS	2.2	5.3 ^d	2005–2007	Table 4, <i>Bock and Nuret</i> [2009]
ECMWF/ZWD	MM5	GPS	2.7	14.3	1999	Table 3, <i>Behrend et al.</i> [2002]
ECMWF/ZWD	MM5	VLBI	10.3	14.3	1999	Table 3, <i>Behrend et al.</i> [2002]
ECMWF/ZTD ^c	\	GPS	\	9.5–13.0 ^d	January 2008 to March 2010	section 3 <i>Cong et al.</i> [2012]
MADIS/ZTD	MM5/LAPS	GPS	10.5	14.3 ^c	June 2004 to August 2007	Table 1, <i>Foster et al.</i> [2013]
RAP or NAM/PWV	WRF	RAOBS	0.33–1.33 (0.63)	1.16–2.65 (1.96)	June 2010 to September 2011	HRRR-AK
RAP or NAM/ZWD	WRF	RAOBS	2.16–8.61 (4.10)	7.57–17.25 (12.72)	June 2010 to September 2011	HRRR-AK
RAP or NAM/ZTD	WRF	RAOBS	2.33–10.92 (5.88)	8.74–17.79 (13.78)	June 2010 to September 2011	HRRR-AK

^aRMS and bias computed from model minus reference data (unit, mm). Last three rows are the statistics of HRRR-AK listed as winter performance-summer performance (average performance).

^bThe statistics of 6 hourly model outputs and the original unit was kg/m² that has been converted to millimeter [*Bevis et al.*, 1992].

^cThe bias of difference and NWP simulate model is not available and its standard deviation listed is as winter-summer.

^dStandard deviation of difference and the others is RMS.

average HRRR-AK model performance of the 24 h model lead time results (see numbers in brackets in the last three rows of Table 9). All HRRR-AK results in Table 9 have already been listed in previous tables. The bias of HRRR-AK PWV estimation is about the same level as NCEP-I and significantly better than that of most other reported models. The overall bias of HRRR-AK in ZWD and ZTD products is similar to other models initialized by ECMWF inputs. The average RMS of HRRR-AK simulation was found to be superior to the RMS of the most of the other models shown in Table 9. Hence, the performance parameters found for HRRR-AK appear realistic in nature and indicate a slightly improved quality of HRRR-AK compared to similar models.

5.2. Summary of Findings

[69] In order to provide a thorough statistical analysis of the performance of the NWP HRRR-AK for atmospheric correction of microwave remote sensing data, this study performed a comparative analysis of atmospheric data from RAOBS measurements with predictions from the HRRR-AK model. Within this research, five test sites were selected over Alaska to cover a wide range of climate types of subarctic and Arctic regions in the U.S. The performance of HRRR-AK in atmospheric artifacts correction for radar signals was assessed by comparing atmospheric parameters from HRRR-AK simulations and radiosonde observations, including vertical precipitable water vapor (PWV) and absolute signal delays. The HRRR-AK accuracy analysis was based on both linear regression models and point-by-point comparisons and utilized error propagation techniques (section 4.1). To assess how the model setup parameters and physical conditions affect the HRRR-AK performance, a series of experiments were designed, analyzing the dependence of prediction performance on model lead times, seasonal effects, as well as sunlight conditions. Our analysis shows that HRRR-AK overestimates the amount of PWV compared to RAOBS observations, indicated by significant deviations of best fitting linear regression slopes from 1 (equation (8)). Uncertainties due to bias ($\mu_{\text{wet,RMS}}$) and random errors of wet delay show a significant reduction of model bias from 6 h to 24 h (Table 2), indicating the

model getting drier when increasing model forecast period. Hence, a precalibration of HRRR-AK products is suggested that is able to reduce this bias. Uncertainties due to random errors (Table 1) showed only little dependency on model lead time. Both the accuracy of simulated PWV delays σ_L ,_{wet} as well as absolute signal delays σ_L showed no significant change with changing model lead times.

[70] At a model lead time of 24 h, the uncertainties σ_{PWV} from random errors computed from HRRR-AK can be predicted with accuracies varying between 1.62 mm and 2.08 mm at different test site. At 6 h lead time, σ_{PWV} is slightly smaller and ranges from 1.31 mm to 1.91 mm (see Table 1). This is within the accuracy level of radiosonde observation itself (1–2 mm) [*Niell et al.*, 2001]. The observed σ_{PWV} corresponds to wet delay uncertainties of $\sigma_{L,\text{wet}} \leq 13.51$ mm for all tested model lead times. The uncertainty of the hydrostatic delay $\sigma_{L,\text{hydro}}$ was determined to be less than 5.4 mm independent of climate region. Although hydrostatic delays dominate the total delay along the radar propagation path, its impact on the uncertainty of the one-way ZWD is relatively small compared to the wet delay influence $\sigma_{L,\text{wet}}$. In summary, for different tested sets and model lead times setting σ_L from random errors can be simulated with an accuracy of better than 14.3 mm (Table 1) with 90% of the errors contributed by water vapor.

[71] An analysis of seasonal influences on HRRR-AK performance used only data with model lead times of 12 h and found that the overall accuracy of one-way total delay predictions in all climate conditions during the local AK winter time (<10.3 mm) is better than the one in local summer (<18.2 mm) as shown in Tables 3 and 4. The regression slope analysis showed that for all regions (with the exception of wintertime data at site PABR), regression slopes were statistically significantly larger than 1, together with the bias listed in Table 5 indicating a PWV overestimation of HRRR-AK relative to RAOBS data. Similar estimation biases were reported in previous studies [*Li et al.*, 2006b; *Mattioli et al.*, 2007]. The causes for the observed PWV overestimation were further analyzed by examining the vertical profiles of the predicted atmospheric parameters Q_v , P , and T (see Figure 5). These analyses suggest that

biases in water vapor mixing ratios Q_v and pressure P are the main reasons for model errors.

[72] An assessment of the dependencies of HRRR-AK performance on sunlight conditions was conducted using stations PANC, PASN, and PANT, which were selected due to their geographic locations. From this study, both daytime and nighttime data showed good linear correlation with RAOBS observations for both PWV and hydrostatic delay predictions (Tables 6 and 7). The estimated average total delay error σ_L from random errors in the nighttime stack was ~ 1 mm smaller than the daytime data.

[73] Regarding the dependence of HRRR-AK on climate conditions, test site PANT, which is the southernmost test site with highest average water vapor records, shows slightly worse linear correlation to RAOBS measurements. This is further evidence that humidity has significant influence on HRRR-AK performance. However, further studies are necessary to study this relationship.

5.3. Error Sources in Methodology of Assessment

[74] Besides the limitations inherent in the HRRR-AK product itself, there are methodology-related issues that may lead to an overestimation of the total HRRR-AK error budget in this study:

[75] 1. *Timing error in data comparison.* The output of the HRRR-AK model can be considered as an instantaneous product that provides simulations of the atmosphere at user defined time steps. However, the radiosonde is recording atmospheric data over time while the balloon is rising from the ground to 15 km asl. This ascent can take up to 1 h [Niell *et al.*, 2001]. This short timing inconsistency may introduce errors mostly into measurements of the highly turbulent atmospheric water vapor.

[76] 2. *Drifting of the radiosonde balloon.* The previous records show that radiosonde can drift as far as 200 km from the point of balloon release [NWS, 2010] as winds may lead to a tilted flight path rather than a rise in zenith direction. As the resolution grid of the HRRR-AK model is 3 km in lateral direction, this may lead to a drift through several model pixels. Since the atmosphere can be considered spatially smooth and the wind speed is much lower near the ground, the introduced errors may not be significant.

[77] 3. *Inaccurate topography records between radiosonde and numerical weather simulations.* Disagreements between the height of the bottommost layer in the HRRR-AK model and the recorded topography height in RAOBS data will introduce residuals in surface pressure estimates that increase the uncertainty of simulated zenith hydrostatic delays. As no significant biases of hydrostatic delays were found, we assume that this error was insignificant for our test sites.

[78] 4. *Errors introduced by the projection function Π .* Π is a projection parameter whose value weakly and inversely depends on the atmospheric surface temperature (see equation (3)). Despite this dependency, a fixed value of $\Pi = 6.5$ was used in this study, corresponding to a surface temperature of 5°C [Bevis *et al.*, 1992]. Specifically, for Alaskan regions with highly variable and deviating climatic conditions, using a constant value for Π could lead to biases. For instance, Π is about 7.2 during the winter period of PABR, which could lead to an underestimation of PWV for this area. Given the low humidity conditions during Alaska winters,

biases of ZWD in the winter season related to errors in Π are still relatively small, e.g., less than 0.5 mm for PABR during winter days with surface temperature of -30°C .

6. Conclusion and Suggestion

[79] Overall, the HRRR-AK products with less than 24 h model lead time can be used for calibrating atmospheric delays in spaceborne SAR systems with an average residual error of less than ~ 13 mm (Table 1 last row) to 14 mm (Table 2 last column). These results are valid for subarctic and arctic conditions. The main performance limitation stems from inaccurate PWV delay predictions, while the error contribution of hydrostatic delay components is small. Consequently, absolute ranging and correlation-based deformation measurements can be corrected with an average residual error of less than ~ 13 to 14 mm. Differential ZTD in InSAR data can be corrected with residual errors of about 20 mm (equation (7)). Atmospheric correction using HRRR-AK data promises better performance during winter months (e.g., from November to May) compared to the period from June to October (summer). For Alaska-type climates, the performance difference between winter and summer is about a factor of 2 (see Tables 3 and 4). The weak correlation between non-systematic errors in ZTD and sunlight conditions suggests that the HRRR-AK product would provide statistically equal performance for atmospheric delay correction in ascending imagery and descending imagery.

[80] **Acknowledgments.** This work was supported by the NASA Headquarters under the NASA Earth and Space Science Fellowship Program—Grant NNX10AO70H. HRRR-AK data were provided by the Arctic Region Supercomputing Center at the University of Alaska Fairbanks. We thank Julie Malinowski, NOAA National Weather Service for providing valuable radiosonde stations information.

References

- Arctic Region Supercomputing Center (ARSC) (2012), ARSC High Resolution Rapid Refresh (HRRR), Arctic Region Supercomputing Center <http://weather.arsc.edu/HRRR/>.
- Behrend, D., R. Haas, D. Pino, L. P. Gradinarsky, S. J. Keihm, W. Schwarz, L. Cucurull, and A. Rius (2002), MM5 derived ZWDs compared to observational results from VLBI, GPS and WVR, *Phys. Chem. Earth, Parts A/B/C*, 27(4–5), 301–308.
- Benson, C., S. A. Bowling, and G. Weller (1983), Urban climates in Alaska, *Environments*, 15(2), 23–26.
- Berardino, P., G. Fornaro, R. Lanari, and E. Sansosti (2002), A new algorithm for surface deformation monitoring based on small baseline differential SAR interferograms, *IEEE Trans. Geosci. Remote Sens.*, 40(11), 2375–2383.
- Bevis, M., S. Businger, T. A. Herring, C. Rocken, R. A. Anthes, and R. H. Ware (1992), GPS meteorology: Remote sensing of atmospheric water vapor using the global positioning system, *J. Geophys. Res.*, 97(D14), 15,787–15,801.
- Bieniek, P. A., et al. (2012), Climate divisions for Alaska based on objective methods, *J. Appl. Meteorol. Climatol.*, 51(7), 1276–1289.
- Bock, O., and M. Nuret (2009), Verification of NWP model analyses and radiosonde humidity data with GPS precipitable water vapor estimates during AMMA, *Wea. Forecasting*, 24(4), 1085–1101.
- Chen, M. H., R. B. Rood, and W. G. Read (1999), Seasonal variations of upper tropospheric water vapor and high clouds observed from satellites, *J. Geophys. Res.*, 104(D6), 6193–6197.
- Cong, X., U. Bals, M. Eineder, and T. Fritz (2012), Imaging geodesy: Centimeter-level ranging accuracy with TerraSAR-X: An update, *IEEE Geosci. Remote Sens. Lett.*, 9(5), 948–952.
- Davis, J. L., T. A. Herring, I. I. Shapiro, A. E. E. Rogers, and G. Elgered (1985), Geodesy by radio interferometry – Effects of atmospheric modeling errors on estimates of baseline length, *Radio Sci.*, 20(6), 1593–1607.
- Dzurisin, D. (2007), *Volcano Deformation: Geodetic Monitoring Techniques*, vol. xxxv, 441 pp., Springer-Praxis Berlin, New York, Chichester, UK.

- Eineder, M., C. Minet, P. Steigenberger, X. Cong, and T. Fritz (2011), Imaging geodesy: Toward centimeter-level ranging accuracy with TerraSAR-X, *IEEE Trans. Geosci. Remote Sens.*, *49*(2), 661–671.
- England, M. N., F. J. Schmidlin, and J. M. Johansson (1993), Atmospheric moisture measurements – A microwave radiometer - radiosonde comparison, *IEEE Trans. Geosci. Remote Sens.*, *31*(2), 389–398.
- Ferretti, A., C. Prati, and F. Rocca (2001), Permanent scatterers in SAR interferometry, *IEEE Trans. Geosci. Remote Sens.*, *39*(1), 8–20.
- Foster, J., J. Kealy, T. Cherubini, S. Businger, Z. Lu, and M. Murphy (2013), The utility of atmospheric analyses for the mitigation of artifacts in InSAR, *J. Geophys. Res. Solid Earth*, *118*, 748–758, doi:10.1002/jgrb.50093.
- Fournier, T., M. E. Pritchard, and N. Finnegan (2011), Accounting for atmospheric delays in InSAR data in a search for long-wavelength deformation in South America, *IEEE Trans. Geosci. Remote Sens.*, *49*(10), 3856–3867.
- Gong, W., F. Meyer, P. Webley, and Z. Lu (2010), Tropospheric correction of InSAR time-series with the weather research forecasting model: An application to volcanic deformation monitoring, paper presented at American Geophysical Union, Fall Meeting 2010, San Francisco.
- Great Britain. Meteorological Office (1991), *Meteorological Glossary*, 6th ed., 335 pp., HMSO, London.
- Hanssen, R. (2001), *Radar Interferometry: Data Interpretation and Error Analysis*, 1st ed., Kluwer Academic Publishers, Netherlands.
- Kampes, B. (2006), *Radar Interferometry: Persistent Scatterer Technique*, 211 pp., Springer, Dordrecht, the Netherlands.
- Kuo, H. L., and W. Y. Sun (1976), Convection in the Lower Atmosphere and its Effects, *J. Atmos. Sci.*, *33*(1), 21–40.
- Li, Z., E. J. Fielding, P. Cross, and J. Muller (2006a), Interferometric synthetic aperture radar atmospheric correction: GPS topography-dependent turbulence model, *J. Geophys. Res.*, *111*, B02404, doi:10.1029/2005JB003711.
- Li, Z., E. J. Fielding, P. Cross, and R. Preusker (2009), Advanced InSAR atmospheric correction: MERIS/MODIS combination and stacked water vapour models, *Int. J. Remote Sens.*, *30*(13), 3343–3363.
- Li, Z., J. P. Muller, P. Cross, P. Albert, J. Fischer, and R. Bennartz (2006b), Assessment of the potential of MERIS near-infrared water vapour products to correct ASAR interferometric measurements, *Int. J. Remote Sens.*, *27*(2), 349–365.
- Liu, L., T. Zhang, and J. Wahr (2010), InSAR measurements of surface deformation over permafrost on the North Slope of Alaska, *J. Geophys. Res.*, *115*, F03023, doi:10.1029/2005JB003711.
- Liu, S., and R. Hanssen (2009), The Atmospheric phase screen: Characteristics and estimation, in *The Troposphere, Ionosphere, GPS, and Interferometric Radar Workshop*, Pasadena, CA, USA.
- Lu, Z., D. Dzurisin, J. Biggs, C. Wicks, and S. McNutt (2010), Ground surface deformation patterns, magma supply, and magma storage at Okmok volcano, Alaska, from InSAR analysis: 1. Interruption deformation, 1997–2008, *J. Geophys. Res.*, *115*, B00B02, doi:10.1029/2009JB006969.
- Mattioli, V., E. R. Westwater, D. Cimini, J. C. Liljegren, B. M. Lesht, S. I. Gutman, and F. J. Schmidlin (2007), Analysis of radiosonde and ground-based remotely sensed PWV Data from the 2004 North Slope of Alaska Arctic winter radiometric experiment, *J. Atmos. Oceanic Technol.*, *24*(3), 415–431.
- Meyer, F., R. Bamler, R. Leinweber, and J. Fischer (2008), A comparative analysis of tropospheric water vapor measurements from MERIS and SAR, paper presented at IEEE International Geoscience and Remote Sensing Symposium, Boston, USA.
- Morton, D., and J. Malingowski (2012), Personal communications in radiosonde equipments in Alaska.
- Niell, A. E., A. J. Coster, F. S. Solheim, V. B. Mendes, P. C. Toor, R. B. Langley, and C. A. Upham (2001), Comparison of measurements of atmospheric wet delay by radiosonde, water vapor radiometer, GPS, and VLBI, *J. Atmos. Oceanic Technol.*, *18*(6), 830–850.
- National Oceanic and Atmospheric Administration (2012), Rapid Refresh (RR), Earth system research laboratory, <http://rapidrefresh.noaa.gov/>.
- National Weather Service (NWS) (2010), National Weather Service Manual 10-1401, Department of Commerce, NOAA, <http://www.nws.noaa.gov/directives/sym/pd01014001curr.pdf>.
- Onn, F., and H. A. Zebker (2006), Correction for interferometric synthetic aperture radar atmospheric phase artifacts using time series of zenith wet delay observations from a GPS network, *J. Geophys. Res.*, *111*, B09102, doi:10.1029/2005JB004012.
- Pacione, R., C. Sciarretta, F. Vespe, C. Faccani, R. Ferretti, E. Fionda, C. Ferraro, and A. Nardi (2001), GPS meteorology: Validation and comparisons with ground-based microwave radiometer and mesoscale model for the Italian GPS permanent stations, *Phys. Chem. Earth Part A*, *26*(3), 139–145.
- Peel, M. C., B. L. Finlayson, and T. A. McMahon (2007), Updated world map of the Koppen-Geiger climate classification, *Hydrol. Earth Syst. Sci.*, *11*(5), 1633–1644.
- Picon, L., R. Roca, S. Serrar, J. L. Monge, and M. Desbois (2003), A new METEOSAT “water vapor” archive for climate studies, *J. Geophys. Res.*, *108*(D10), 4301, doi:10.1029/2002JD002640.
- Resch, G. M. (1980), *Water Vapor - The Wet Blanket of Microwave Interferometry*, Academic Press, New York.
- Richter, J. H., and H. V. Hitney (1980), *The Effects of Atmospheric Refractivity on Microwave Propagation*, Academic Press, New York.
- Searby, H. W. (1968), *Climates of the States: Alaska*, 23 pp, U.S. Department of Commerce.
- Segall, P. (2010), *Earthquake and volcano deformation*, vol. xxiii, 458 pp., Princeton University Press, Princeton, N.J.
- Skamarock, W. C. (2004), Evaluating mesoscale NWP models using kinetic energy spectra, *Mon. Weather Rev.*, *132*(12), 3019–3032.
- Skamarock, W. C., J. B. Klemp, J. Dudhia, D. Gill, D. Barker, K. G. Duda, X. Huang, W. Wang, and J. G. Powers (2008), A description of the Advanced Research WRF Version 3, NCAR Technical Note NCAR/TN-468+STR, pp. 83–83.
- Sleep, N. H., and K. Fujita (1997), *Principles of geophysics*, vol. xviii, 586 pp., Blackwell Science, Malden, Mass., USA.
- Smith, E. K., and S. Weintraub (1953), The constants in the equation for atmospheric refractive index at radio frequencies, *Proc. IRE*, *41*(8), 1035–1037.
- Stafford, J. M., G. Wendler, and J. Curtis (2000), Temperature and precipitation of Alaska: 50 year trend analysis, *Theor. Appl. Climatol.*, *67*(1–2), 33–44.
- Stone, R. S., E. G. Dutton, J. M. Harris, and D. Longenecker (2002), Earlier spring snowmelt in northern Alaska as an indicator of climate change, *J. Geophys. Res.*, *107*(D10), 4089, doi:10.1029/2000JD000286.
- University of Wyoming (2012), Atmospheric Sounding, University of Wyoming, College of Engineering, Department of Atmospheric Science, <http://weather.uwyo.edu/upperair/sounding.html>.
- Wang, C., D. Wilson, T. Haack, P. Clark, H. Lean, and R. Marshall (2011), Effects of initial and boundary conditions of mesoscale models on simulated atmospheric refractivity, *J. Appl. Meteorol. Climatol.*, *51*(1), 115–132.
- Wang, J., and L. Zhang (2008), Systematic errors in global radiosonde precipitable water data from comparisons with ground-based GPS measurements, *J. Clim.*, *21*(10), 2218–2238.
- Webley, P. W., R. M. Bingley, A. H. Dodson, G. Wadge, S. J. Waugh, and I. N. James (2002), Atmospheric water vapour correction to InSAR surface motion measurements on mountains: Results from a dense GPS network on Mount Etna, *Phys. Chem. Earth*, *27*(4–5), 363–370.
- Wei, M., D. Sandwell, and B. Smith-Konter (2010), Optimal combination of InSAR and GPS for measuring interseismic crustal deformation, *Adv. Space Res.*, *46*(2), 236–249.
- Xu, W. B., Z. W. Li, X. L. Ding, and J. J. Zhu (2011), Interpolating atmospheric water vapor delay by incorporating terrain elevation information, *J. Geodesy*, *85*(9), 555–564.